Thermodynamic properties of ε-Fe with thermal electronic excitation effects on vibrational spectra

Jingyi Zhuang,[1,2] Hongjin Wang,[3,4] Qi Zhang,[4] and Renata M. Wentzcovitch[1,2,4,*]

[1]*Department of Earth and Environmental Sciences, Columbia University, New York, New York 10027, USA*
[2]*Lamont–Doherty Earth Observatory, Columbia University, Palisades, New York 10964, USA*
[3]*Department of Computer Sciences, Columbia University, New York, New York 10027, USA*
[4]*Department of Applied Physics and Applied Mathematics, Columbia University, New York, New York 10027, USA*

(Received 18 December 2020; revised 21 February 2021; accepted 16 March 2021; published 12 April 2021)

The thermodynamic properties of hexagonal-close-packed iron (ε-Fe) are essential for investigating the internal structure and dynamic properties of planetary cores. Despite their importance to planetary sciences, experimental investigations of ε-Fe at relevant conditions are still challenging. Therefore, *ab initio* calculations are crucial to elucidating the thermodynamic properties of this system. Here, we use a free energy calculation scheme based on the phonon gas model compatible with temperature-dependent phonon frequencies. We investigate the effects of electronic thermal excitations, which introduces a temperature dependence on phonon frequencies, and the implication for the thermodynamic properties of ε-Fe at extreme pressure (P) and temperature (T) conditions. We disregard phonon-phonon interactions, i.e., anharmonicity and their effect on phonon frequencies. Nevertheless, the current scheme is also applicable to T-dependent anharmonic frequencies. We conclude that the impact of thermal electronic excitations on vibrational properties is not significant up to ∼4000 K at 200 GPa but should not be ignored at higher temperatures or pressures. However, the static free energy F_{st} must always include the effect of thermal excitation fully in a continuum of T. Our results for isentropic equations of state show good agreement with data from recent ramp compression experiments up to 1400 GPa conducted at the National Ignition Facility.

DOI: 10.1103/PhysRevB.103.144102

I. INTRODUCTION

Hexagonal-close-packed (hcp) iron (ε-Fe) is the likely stable phase of iron at the extreme conditions of terrestrial solar and extrasolar planetary cores [1]. Its thermodynamic properties are essential for modeling this region and the mantle above it. There are numerous pioneering theoretical and experimental studies of the properties of ε-Fe. Previous *ab initio* calculations of ε-Fe have been carried out using various techniques, e.g., quantum Monte Carlo (QMC) [2], all-electron methods [3], pseudopotential methods [4–9], and molecular dynamics (MD) [10]. Experimental investigations of equations of state (EoS) of ε-Fe include static compression in diamond anvil cell (DAC) [11–13] and dynamic compression experiments [14,15] up to 300 GPa. A recent ramp compression experiment [16] measured the density-pressure relation in ε-Fe up to 1.4 TPa at unconstrained temperatures. Planetary cores reach very high temperatures, e.g., ∼6000 K at ∼365 GPa in the Earth [17], and isothermal compression results are also significant. Recent modeling of terrestrial exoplanets with up to 20 Earth masses [18] shows that pressures and temperatures at the center of these planets and identified phases can reach over 13 TPa and 9000 K. These conditions remain challenging also for computations of solid-state properties as such high temperatures bring extra complexity, e.g., anharmonicity, electronic thermal excitations, and likely atomic diffusion [19]. In previous *ab initio* studies [8,20–22], some of these effects were not fully considered, or their implications were not analyzed. Here, we investigate the influence of electronic excitations alone on the vibrational and thermodynamic properties of ε-Fe. Like phonon-phonon interaction, it produces temperature-dependent (T-dependent) phonon frequencies that also affect free energy calculations.

Thermodynamic properties of ε-Fe addressing these complex effects have been discussed in some previous *ab initio* studies. Unavoidably, results differ somewhat because of multiple methodologies used [5,6,22]. Among the popular methods, the quasiharmonic approximation (QHA) is appropriate for addressing these properties in weakly anharmonic solids up to $\sim\frac{2}{3}$ of the melting temperature in most cases. It is computationally less demanding than MD. It requires only calculations of the vibrational density of states (VDoS) at about 10 pressures. Such calculations are more challenging for metals where electronic thermal excitations may affect phonon frequencies [23].

Hence, we implemented a free energy calculation scheme based on the phonon gas model (PGM) compatible with T-dependent phonon or phonon quasiparticle frequencies to investigate ε-Fe at planetary interior conditions. The present calculation disregards phonon-phonon interaction effects, i.e., anharmonicity, but addresses directly and precisely the unavoidable impact of electronic thermal excitations on phonon dispersions and thermodynamic properties of metals. Nonetheless, the present scheme is also applicable to free energy computations when phonon-phonon interactions

*rmw2150@columbia.edu

are nonnegligible and the T dependence of phonon quasiparticle frequencies originates in anharmonicity [21,24]. The current implementation offers properties in a continuum range of states up to ultra-high temperatures and pressures [24]. Here, we present thermodynamic properties of ε-Fe covering a wide range of pressures (0–1400 GPa) and temperatures (0–8000 K). We investigate the interplay between electronic thermal excitations and vibrational properties and the effect it plays on thermodynamic properties. Results for the isentropic EoS of ε-Fe are in good agreement with data from recent ramp compression experiments up to 1400 GPa conducted at the National Ignition Facility (NIF) [16].

This paper is organized as follows. In the next section, we introduce the *ab initio* simulation details and the PGM formalism. The following section shows results and compares them with experimental data and previous calculations. We summarize our conclusions in the last section.

II. METHODS

A. Phonon gas model (PGM)

The PGM assumes phonons or phonon quasiparticles do not interact. Within the Born–Oppenheimer approximation and for harmonic systems, the PGM free energy is given by the QHA:

$$F(V,T) = F_{\rm st}(V) + F_{\rm vib}(V,T), \tag{1a}$$

For insulators,

$$F_{\rm st}(V) = E_{\rm KS}(V), \tag{1b}$$

where $F_{\rm st}(V)$ is the static free energy, with $E_{\rm KS}(V)$ being the Kohn–Sham energy for an equilibrium ionic configuration with static equilibrium volume V.

$$F_{\rm vib}(V,T) = \frac{1}{2}\sum_{\mathbf{q},s}\hbar\omega_{\mathbf{q},s}(V) + k_BT\sum_{\mathbf{q},s}\ln\left[1-\exp\left(-\frac{\hbar\omega_{\mathbf{q},s}(V)}{k_BT}\right)\right], \tag{1c}$$

is the vibrational free energy with $\omega_{\mathbf{q},s}(V)$ being the vibrational frequency of noninteracting phonons with wavenumber $\mathbf{q}$ and polarization index s, and $T = T_{\rm ion}$ the ionic temperature. The first and second terms on the right-hand side of Eq. (1c) are the zero-point $E_{\rm zp}(V)$ and thermal vibrational free energy $E_{\rm th}(V,T)$, respectively. In this approximation, $\omega_{\mathbf{q},s}(V)$ is T independent, depending only on V. The corresponding entropy of this system is

$$S_{\rm vib}(V,T) = k_B\sum_{\mathbf{q},s}[(1+n_{\mathbf{q}s})\ln(1+n_{\mathbf{q}s}) - n_{\mathbf{q}s}\ln n_{\mathbf{q}s}], \tag{1d}$$

where the normal mode population $n_{\mathbf{q}s}(V,T)$ is

$$n_{\mathbf{q}s}(V,T) = \frac{1}{\exp\frac{\hbar\omega_{\mathbf{q}s}(V)}{k_BT}-1}. \tag{1e}$$

For metallic systems with negligible anharmonicity (phonon-phonon interactions), the static energy $F_{\rm st}$ and vibrational frequencies should be computed with the Mermin functional [25,26], i.e., the finite temperature version of density functional theory (DFT). In this case, phonon frequencies acquire a T dependence through thermal electronic excitation at a temperature $T_{\rm el}$ [23]. For clarity's sake, we now distinguish $T_{\rm el}$ and $T_{\rm ion}$ to identify the origin of the T dependence in the calculation. Obviously, $T_{\rm el} = T_{\rm ion} = T$ when the system is in thermodynamic equilibrium. A common, although approximate, expression for the free energy in this case

$$F(V,T_{\rm el},T_{\rm ion}) = F_{\rm st}(V,T_{\rm el}) + F_{\rm vib}(V,T_{\rm el},T_{\rm ion}), \tag{2a}$$

where

$$F_{\rm st}(V,T_{\rm el}) = F_{\rm Mermin}(V,T_{\rm el}), \tag{2b}$$

is the total Mermin free energy for an equilibrium ionic configuration at volume V. Here,

$$F_{\rm Mermin}(V,T_{\rm el}) = E_{\rm st}(V,T_{\rm el}) - T_{\rm el}S_{\rm el}(V,T_{\rm el}), \tag{2c}$$

where $E_{\rm st}(V,T_{\rm el})$ is the self-consistent energy with orbital occupancies

$$f_{\mathbf{k}i}(V,T_{\rm el}) = \frac{1}{\exp\frac{\hbar(E_{\mathbf{k}i}-E_F)}{k_BT_{\rm el}}+1}, \tag{2d}$$

with $E_{\mathbf{k}i}$ being the one-electron energy of an orbital with wavenumber $\mathbf{k}$ and band index i, and E_F being the Fermi energy. The electronic entropy is

$$S_{\rm el}(V,T_{\rm el}) = -k_B\sum_{\mathbf{k},i}[(1-f_{\mathbf{k}i})\ln(1-f_{\mathbf{k}i}) + f_{\mathbf{k}i}\ln f_{\mathbf{k}i}]. \tag{2e}$$

The vibrational energy is

$$F_{\rm vib}(V,T_{\rm el},T_{\rm ion}) = \frac{1}{2}\sum_{\mathbf{q},s}\hbar\omega_{\mathbf{q},s}(V,T_{\rm el}=0) + k_BT_{\rm ion}\sum_{\mathbf{q},s}\ln\left\{1-\exp\left[-\frac{\hbar\omega_{\mathbf{q},s}(V,T_{\rm el})}{k_BT_{\rm ion}}\right]\right\}, \tag{2f}$$

and the vibrational entropy is

$$\begin{aligned} S_{\rm vib}(V,T_{\rm el},T_{\rm ion}) &= -\left.\frac{\partial F(V,T_{\rm el},T_{\rm ion})}{\partial T_{\rm ion}}\right|_{T_{\rm el},V} - \left.\frac{\partial F(V,T_{\rm el},T_{\rm ion})}{\partial T_{\rm el}}\right|_{T_{\rm ion},V} \\ &= k_B\sum_{\mathbf{q},s}[(1+n_{\mathbf{q}s})\ln(1+n_{\mathbf{q}s}) - n_{\mathbf{q}s}\ln n_{\mathbf{q}s}] \\ &\quad - \sum_{\mathbf{q},s} n_{\mathbf{q}s}\hbar\omega'_{\mathbf{q},s}(V,T_{\rm el}), \end{aligned} \tag{2g}$$

with $\omega'_{\mathbf{q},s}(V,T_{\rm el}) = \frac{\partial\omega_{\mathbf{q}s}(V,T_{\rm el})}{\partial T_{\rm el}}|_{T_{\rm ion},V}$, and

$$n_{\mathbf{q}s}(V,T_{\rm el},T_{\rm ion}) = \frac{1}{\exp\frac{\hbar\omega_{\mathbf{q}s}(V,T_{\rm el})}{k_BT_{\rm ion}}-1}. \tag{2h}$$

This type of calculation has previously been carried out for various systems, e.g., Fe [8] and Pt [27]. While $F_{\rm st}(V,T_{\rm el})$ has

TABLE I. Free energy computation schemes used in this paper.

Scheme	Name	Free energy calculations: Formalism	T_{el} effect on F_{st}	T_{el} effect on F_{vib}	Validity
EIM	Entropy integration method	Eqs. (4a)–(4e)	Yes	Yes	Anharmonic and nearly harmonic metals and insulators
TQHA	Temperature-dependent quasiharmonic approximation	Eqs. (2a)–(2h)	Yes	Yes	Good approximation for nearly harmonic metals and insulators
TIP	Temperature-independent phonons	Eqs. (4a)–(4e)	Yes	No	Good approximation for nearly harmonic metals and insulators
QHA	Quasiharmonic approximation	Eqs. (1a)–(1c)	No	No	Nearly harmonic insulators

always been computed in a continuum T_{el} range, $\omega_{\mathbf{q}s}(V, T_{el})$ has often been computed at a single T_{el}, e.g., 300 K. As will be illustrated below, this approximation is satisfactory for nearly harmonic systems without rapidly varying electronic density of states at the Fermi level. In this case, $\omega_{\mathbf{q},s}(V, T_{el})$ in Eq. (2g) may be negligible. While this procedure is a natural extension of the QHA to metallic systems, it is not correct because the vibrational entropy in Eq. (2g) differs from that in Eq. (1d), and the second term on the right-hand side of Eq (2g) might be nonnegligible. Equation (1d) should always hold whether the system has T-independent or T-dependent frequencies [28,29].

For anharmonic insulators, the T dependence of phonon frequencies originates in phonon-phonon interactions, i.e., anharmonicity. In this case, one replaces interacting phonons with noninteracting phonon quasiparticles with renormalized T-dependent frequencies $\tilde{\omega}_{\mathbf{q}s}(V, T_{ion})$ and lifetimes $\tau_{\mathbf{q}s}(V, T_{ion})$. The expressions for the particle population in Eq. (1e) and entropy in Eq. (1d) are still valid in this case [23,28,29]. Therefore, the entropy calculation should precede the free energy calculation. The free energy is obtained by integrating the entropy in this case. For an insulating system,

$$F(V, T_{ion}) = F_{st}(V, T_{ion} = 0) + F_{vib}(V, T_{ion}), \tag{3a}$$

where $F_{st}(V,\ T_{ion} = 0)$ is the static free energy at $T = 0$, and

$$F_{vib}(V, T_{ion}) = F_{zp}(V, T_{ion} = 0) - \int_0^{T_{ion}} S_{vib}(V, T')dT', \tag{3b}$$

with $S_{vib}(V, T_{ion})$ given by Eq. (1d) with T-dependent frequencies, i.e.,

$$n_{\mathbf{q}s}(V, T_{ion}) = \frac{1}{\exp\frac{\hbar\tilde{\omega}_{\mathbf{q}s}(V,T_{ion})}{k_B T_{ion}} - 1}. \tag{3c}$$

For metallic anharmonic systems,

$$F(V, T_{el}, T_{ion}) = F_{st}(V, T_{el}) + F_{vib}(V, T_{el}, T_{ion}), \tag{4a}$$

with $F_{st}(V, T_{el})$ given by Eq. (2c), and

$$F_{vib}(V, T_{el},\ T_{ion}) = F_{zp}(V, T_{el} = 0, T_{ion} = 0) - \int_0^{T_{ion}} S_{vib}(V, T_{el} = T', T_{ion} = T')dT', \tag{4b}$$

where

$$S_{vib}(V, T_{el}, T_{ion}) = k_B \sum_{\mathbf{q},s} [(1 + n_{\mathbf{q}s})\ln(1 + n_{\mathbf{q}s}) - n_{\mathbf{q}s} \ln n_{\mathbf{q}s}], \tag{4c}$$

with $n_{\mathbf{q}s}$ given by

$$n_{\mathbf{q}s}(V, T_{ion}, T_{el}) = \frac{1}{\exp\frac{\hbar\tilde{\omega}_{\mathbf{q}s}(V,T_{ion},T_{el})}{k_B T_{ion}} - 1}. \tag{4d}$$

The total entropy of the metallic anharmonic system then is

$$S_{tot}(V, T_{el}, T_{ion}) = S_{el}(V, T_{el}) + S_{vib}(V, T_{el}, T_{ion}), \tag{4e}$$

where $S_{el}(V, T_{el})$ given by Eq. (2e) is included in $F_{st}(V, T_{el})$ in Eq. (4a).

In this paper, we compute the free energy of ε-Fe using Eqs. (2) and (4) and compare their results. We refer to the scheme in Eq. (4) as the entropy integration method (EIM) and to the scheme in Eq. (2) as the T-dependent QHA (TQHA). We show that the T_{el} dependence of the frequencies is weak, rendering the second term on the right-hand side of Eq. (2g) negligible, which makes both procedures practically equivalent. When this is the case, it is acceptable to neglect altogether the T_{el} dependence of phonon frequencies, as done in the past (e.g., Ref. [8]). However, the T_{el} dependence of the static free energy $F_{st}(V, T_{el})$ is crucial for obtaining accurate thermodynamic properties, especially the thermal expansivity [30]. We refer to this scheme as the temperature-independent phonon (TIP). We also investigate a fourth scheme in which free energies and thermodynamic properties are obtained with constant $T_{el} =$ cte. Neither $F_{st}(V, T_{el})$ or phonon frequencies are T_{el} dependent in this case. We refer to this scheme simply as QHA. These four schemes are summarized in Table I.

B. Simulation details

All calculations are performed using the Mermin functional [23,25,26] as implemented in the QUANTUM ESPRESSO [31] software. We use several available pseudopotential and projector augmented wave (PAW) datasets [32–34], including the evolutionary PAW (EPAW) dataset [32] as our primary choice, to investigate the isentropic EoS of ε-Fe up to 1400 GPa and 8000 K. As we focus

on high pressure and temperature conditions, we conduct spin-unpolarized calculations. We use the Perdew–Burke–Ernzerhof generalized gradient approximation (PBE-GGA) [35] for the exchange and correlation functional. We choose a $10 \times 10 \times 10$ Monkhorst-Pack [36] **k**-point mesh and cutoff energy of 1200 eV. Equilibrium structures at several electronic temperatures T_{el} and several static pressures are optimized using the damped variable cell-shape MD [37,38] method. We choose $T_{el} = 0$, 300 K, and from 1000 to 8000 K in steps of 1000 K. For each T_{el}, structures are optimized, and the VDoS computed at the following pressures: between 0 and 300 GPa in steps of 50 GPa, between 300 and 400 GPa in steps of 20 GPa, and between 500 and 1500 GPa in steps of 100 GPa. We calculate phonons on a $4 \times 4 \times 4$ **q**-point mesh, using density functional perturbation theory (DFPT) [39]. Brillouin zone integration for entropy and free energy calculations is performed over a $10 \times 10 \times 10$ **q**-point mesh.

When using the EIM scheme expressed in Eqs. (4a)–(4e), for each V and T_{el}, the vibrational entropy is calculated for T_{ion} varying from 0 to 8000 K in steps of 10 K. This entropy is then interpolated for T_{el} on the same T_{ion} grid using a spline interpolation. At each volume and $T_{el} = T_{ion}$, the free energy is obtained using Eqs. (4a)–(4e). The free energy is then interpolated in V using a third-order finite strain (Birch–Murnaghan) EoS. When using the TQHA scheme, i.e., Eqs. (2a)–(2h), the free energy is computed directly on the same T_{el}, T_{ion}, and V grids and then interpolated for T_{el} and V as done in the EIM scheme. We also use the TIP scheme, i.e., the EIM approach with T-independent phonon frequencies. For comparison, we also compute free energies simply using the QHA [Eqs. (1a)–(1c)] scheme with $T_{el} = \text{cte}$. These four schemes—EIM, TQHA, TIP, and QHA—help to elucidate the impact of T_{el} and T_{ion} on vibrational and thermodynamic properties. They are summarized in Table I. We compute thermodynamic properties using some modules of the QHA Python package [40] after obtaining free energies with these four schemes.

III. RESULTS AND DISCUSSIONS

A. Helmholtz free energy and entropy

As indicated in Sec. II, the PGM framework addresses four distinct situations: (i) harmonic insulators, (ii) metals, (iii) anharmonic insulators, and (iv) anharmonic metals. Except for (i), all other cases have T-dependent frequencies. Free energy computations using the EIM approach is appropriate for all cases, but in principle, it is necessary for cases (ii) to (iv). Here, we also explore the performance of the TQHA approach, i.e., Eq. (2).

Figure 1 shows the VDoS of ε-Fe for different T_{el}. Each VDoS is calculated for structures optimized at 360 GPa (static pressure), which vary slightly with T_{el}. These VDoS do not differ drastically, suggesting a potentially weak dependence of the vibrational free energy on T_{el}. Figure 2 shows the entropy and free energy of ε-Fe produced by the EIM and TQHA approaches. Here, $S_{el}(T)$ and $F_{st}(T)$ [Eqs. (2e) and (2c)] are computed the same way in both approaches, but results differ in the way $S_{vib}(T)$ and $F_{vib}(T)$ are computed, i.e., using Eqs. (2g) and (2f) (TQHA) or Eqs. (4c) and (4b) (EIM). The negative T derivative of $F_{vib}^{TQHA}(T)$ gives $S_{vib}^{TQHA}(T)$ [Eqs. (2f) and (2g)], while the negative integration of $S_{vib}^{EIM}(T)$ gives $F_{vib}^{EIM}(T)$ [Eqs. (4c) and (4b)].

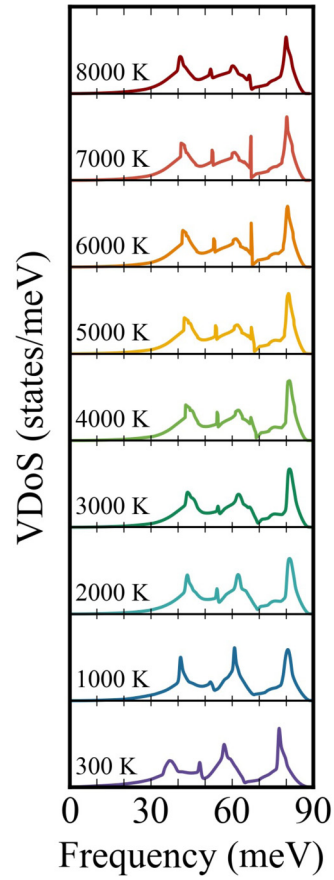

FIG. 1. Vibrational density of states of hexagonal-close-packed (hcp) iron optimized at various electronic temperatures T_{el} at 360 GPa.

The dotted red lines in Figs. 2(a) and 2(b) display $S_{el}(T)$ [Eq. (2e)] and $F_{st}(T)$ [Eq. (2c)], respectively. Dashed colored lines display $S_{vib}^{T_{el}=\text{cte}}(T)$ [Eqs. (2g) and (2h)] and $F_{vib}^{T_{el}=\text{cte}}(T)$ [Eqs. (2f) and (2h)], the latter being shifted by a constant $-F_0$, the total static energy at $T_{el} = 0$. Colored circles are $S_{tot}^{TQHA}(T) = S_{el}(T) + S_{vib}^{T_{el}=T}(T)$ [Eqs. (2e) and (2g)] and $F_{tot}^{TQHA} = F_{st}(T) + F_{vib}^{T_{el}=T}(T) - F_0$ [Eqs. (2a)–(2f)]. Solid black lines are $S_{tot}^{EIM}(T) = S_{el}(T) + S_{vib}^{EIM}(T)$ [Eqs. (2e), (4c), and (4e)] and $F_{tot}^{EIM} = F_{st}(T) + F_{vib}^{EIM}(T) - F_0$ [Eqs. (4a) and (4b)]. As can be seen, $S_{vib}^{T_{el}=\text{cte}}(T)$ depends very weakly on T_{el}, while $F_{vib}^{T_{el}=\text{cte}}(T)$ is slightly more sensitive to it. Nevertheless, $S_{tot}^{EIM}(T) \cong S_{tot}^{TQHA}(T)$, indicating that the last term on the right-hand side of Eq. (2g) is relatively insignificant in the case of ε-Fe and likely other metals as well. Also, $F_{tot}^{EIM}(T) \cong F_{tot}^{TQHA}(T)$ for ε-Fe. The similarity of these quantities appears to justify the use of a single VDoS in calculations of $F_{vib}(V, T)$ or $S_{vib}(V, T)$ for ε-Fe (TIP scheme).

B. Vibrational properties

The vibrational entropy S_{vib} needs special attention since any uncertainty in S_{vib} propagates to other properties via the entropy integration in the EIM approach. Figure 3 shows a

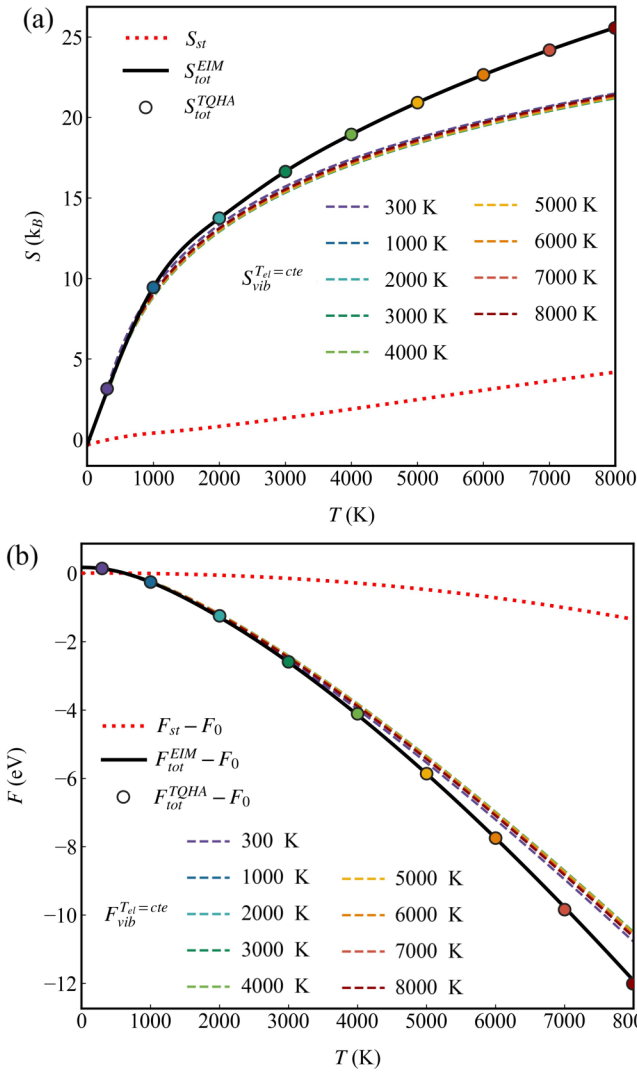

FIG. 2. (a) Entropy at constant volume ($V = 6.77$ Å^3/atom). Dotted red line: $S_{\rm el}(T_{\rm el} = {\rm T})$ [Eqs. (2d) and (2e)]. Dashed colored lines: $S_{\rm vib}^{T_{\rm el}={\rm cte}}(T_{\rm ion} = T)$ [Eq. (2g)]. Colored circles: $S_{\rm tot}^{\rm TQHA}(T) = S_{\rm el}(T_{\rm el} = T) + S_{\rm vib}^{T_{\rm el}=T}(T_{\rm ion} = T)$. Solid black line: $S_{\rm tot}^{\rm EIM}(T_{\rm el} = T_{\rm ion} = T)$ [Eqs. (4c) and (4d)]. (b) Free energy at the same V. Dotted red line: $F_{\rm st}(T_{\rm el} = T) - F_0$ [Eq. (2c)], where $F_0 = -8913.5$ eV is the static energy at $T = 0$ K. Dashed colored lines: $F_{\rm vib}^{T_{\rm el}={\rm cte}}(T_{\rm ion} = T)$ [Eqs. (2a), (2b), and (2f)] at various $T_{\rm el}$. Colored circles: $F_{\rm tot}^{\rm TQHA} = F_{\rm st}(T_{\rm el} = T) + F_{\rm vib}^{T_{\rm el}=T}(T_{\rm ion} = T) - F_0$ [Eqs. (2a)–(2h)]. Solid black line: $F_{\rm tot}^{\rm EIM} = F_{\rm st}(T_{\rm el} = T) + F_{\rm vib}(T_{\rm el} = T_{\rm ion} = T) - F_0$ [Eqs. (4a) and (4b)].

comparison between $S_{\rm vib}^{\rm EIM}(P, 300\ {\rm K})$ and several experimental datasets of this quantity. All $S_{\rm vib}^{\rm exp}(P, 300\ {\rm K})$ shown in Fig. 3 were estimated using VDoS obtained by nuclear resonant inelastic x-ray scattering (NRIXS) [41–45] and Eq. (1d) or Eq. (4c). The electronic entropy $S_{\rm el}$ does not contribute explicitly to $S_{\rm vib}$.

A rapid decrease in $S_{\rm vib}^{\rm exp} \sim 13$ GPa is generally attributed to the phase transition between α-Fe [body centered cubic (bcc)] and ε-Fe (hcp) [13,46]. Here, $S_{\rm vib}^{\rm EIM}(P,\ 300\ {\rm K})$ agrees very well with all the reported NRIXS data, especially with the more recent one by Murphy *et al.* [45] at higher pressures.

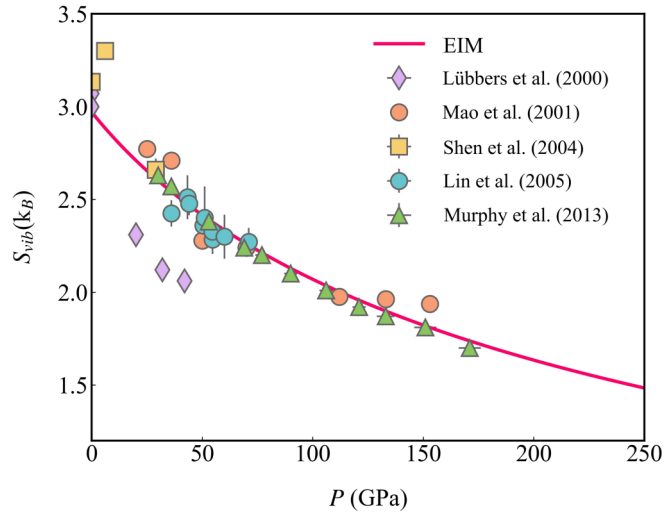

FIG. 3. Vibrational entropy of ε-Fe at $T_{\rm el} = T_{\rm ion} = 300$ K. The solid line is $S_{\rm vib}^{\rm EIM}(P, T = 300\ {\rm K})$ [Eq. (4c)] and symbols are experimental values $S_{\rm vib}^{\rm exp}(P, 300\ {\rm K})$, obtained using Eq. (1d) and vibrational densities of states (VDoS) measured by nuclear resonant inelastic x-ray scattering (NRIXS) [41–45].

At lower pressures ($P \leqslant 50$ GPa), $S_{\rm vib}^{\rm EIM}(P,\ 300\ {\rm K})$ deviates slightly from $S_{\rm vib}^{\rm exp}(P,\ 300\ {\rm K})$. This is likely related to errors in the calculation of the exchange-correlation energy. As shown in the following section (Fig. 7), the 300 K compression curve of ε-Fe is not well reproduced computationally at low pressures. Despite this issue, our vibrational entropy agrees well with available experimental data which also show considerable uncertainty.

The vibrational pressure $P_{\rm vib}(V, T)$, calculated as $-(\frac{\partial F_{\rm vib}}{\partial V})_T$, captures more clearly the $T_{\rm el}$ dependence of the VDoS. Figure 4 compares $P_{\rm vib}^{\rm EIM}(V, T = {\rm cte})$ and $P_{\rm vib}^{\rm TQHA}(V,\ T = {\rm cte})$ with $P_{\rm vib}^{\rm exp}(V, T = {\rm cte})$. The latter was estimated first using VDoS measured with NRIXS [47], followed by calculations of $F_{\rm vib}^{\rm exp}$ and $-(\frac{\partial F_{\rm vib}}{\partial V})_T$, all at 300 K. This is the same procedure used in the calculation of $P_{\rm vib}^{\rm EIM}(V, T = {\rm cte})$. The reported $P_{\rm vib}^{\rm exp}(V,\ T)$ [47] was modeled using the measured $P_{\rm vib}^{\rm exp}(V,\ 300\ {\rm K})$ and first extending it linearly to high T and reported as the harmonic part $P_{\rm vib}^{\rm h}(V,\ T)$. The anharmonic contribution was modeled [13] using *ab initio* anharmonic free energy calculations [48] with $P_{\rm vib}^{\rm anh}(V,\ T)$ fit to a phenomenological formulation [49]. Therefore, $P_{\rm vib}^{\rm exp}(V, T) = P_{\rm vib}^{\rm h}(V, T) + P_{\rm vib}^{\rm anh}(V, T)$. Here, we see EIM and TQHA results are almost indistinguishable, meaning the $T_{\rm el}$ dependence of phonon frequencies is small and could be disregarded, as will be done in Figs. 5 and 6 by comparing EIM and TIP results. Here, $P_{\rm vib}^{\rm exp}$ agrees equally well with $P_{\rm vib}^{\rm EIM}$ and $P_{\rm vib}^{\rm TQHA}$ up to 4000 K, suggesting the anharmonic contribution, disregarded in our calculations, is negligible. At 5600 K, we notice a deviation from $P_{\rm vib}^{\rm exp}$, which suggests anharmonic effects are important at this temperature and beyond. Figure 4 also shows QHA results, meaning $F_{\rm st}(V, T)$ and $F_{\rm vib}(V, T)$ are both computed using $T_{\rm el} = {\rm cte}$, as indicated. This type of calculation is not uncommon for practical comparisons with experimental data at specific temperatures. At 5600 K, QHA results are not available

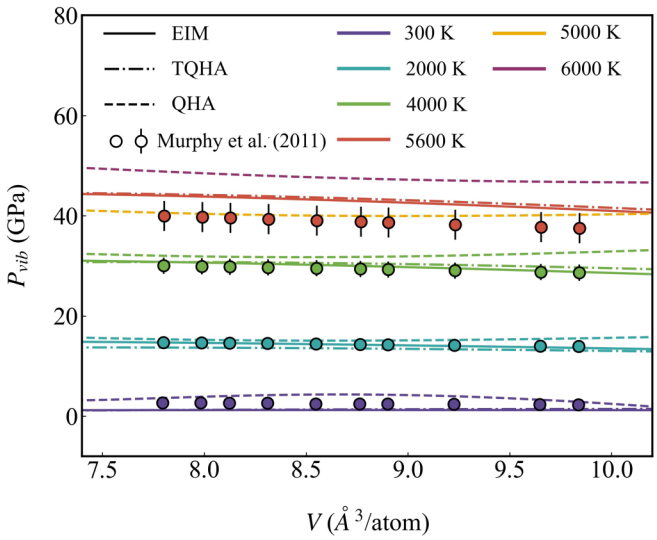

FIG. 4. Vibrational pressure of ε-Fe. Solid lines are $P_{\rm vib}^{\rm EIM}(V,T)$; dashed lines are quasiharmonic approximation (QHA) calculations at $T_{\rm el}$ = cte (see text); dash-dotted lines are $P_{\rm vib}^{\rm TQHA}(V,T)$. QHA results are not available at 5600 K because we did not generate vibrational densities of states (VDoS) at $T_{\rm el} = 5600$ K, but they are bracketed by 5000 and 6000 K values. Symbols are $P_{\rm vib}^{\rm exp}(V,T)$ obtained from VDoS measured using nuclear resonant inelastic x-ray scattering (NRIXS) [47] at 300 K and modeled harmonic and anharmonic contributions at higher T. See text.

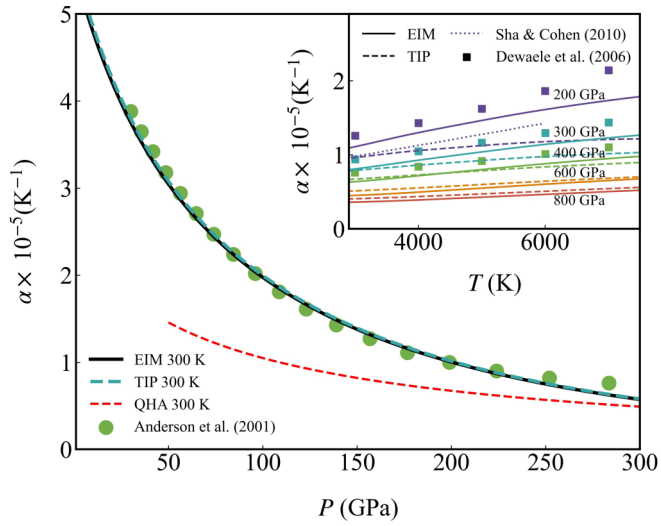

FIG. 5. Thermal expansion coefficient of ε-Fe at 300 K. $\alpha^{\rm EIM}(P, 300\ {\rm K})$ (solid black line) and $\alpha^{\rm TIP}(P, 300\ K)$ (dashed blue line) are quite similar, indicating the low impact of a variable $T_{\rm el}$ on the vibrational free energy $F_{\rm vib}$. The difference between $\alpha^{\rm EIM}(P, 300\ {\rm K})$ and $\alpha^{\rm QHA}(P, 300\ {\rm K})$ (dashed red line) reveals the significant impact of the variable $T_{\rm el}$ in the static free energy $F_{\rm st}$ computed using the Mermin functional. As expected, $\alpha^{\rm EIM}(P, 300\ {\rm K})$ agrees best with $\alpha^{\rm exp}(P, 300\ {\rm K})$ (green circles) [50]. Inset: solid lines are $\alpha^{\rm EIM}(P = {\rm cte},\ T)$ and dashed lines are $\alpha^{\rm TIP}(P = {\rm cte}, T)$ obtained using the vibrational densities of states (VDoS) computed with $T_{\rm el} = 300$ K. Dotted lines are *ab initio* results by Sha and Cohen [4]. Squares are semi-empirically modeled [60] experimental data obtained in diamond anvil cell (DAC) experiments [13].

since we do not have phonons with $T_{\rm el} = 5600$ K, but we show QHA results at 5000 and 6000 K for comparison. The discrepancy between QHA and EIM/TQHA results indicates the importance of properly computing the static free energy $F_{\rm st}(V, T_{\rm el})$ in a continuum (fine grid) of $T_{\rm el} = T_{\rm ion}$. As pointed out above, the agreement between EIM and TQHA results indicates that the effect $T_{\rm el}$ on $F_{\rm vib}(T, V)$ is negligible in ε-Fe. The origin of the deviation of QHA results from EIM/TQHA is clarified in the next calculation of thermal expansivity at 300 K.

C. Thermal expansion coefficient

The thermal expansion coefficient $\alpha = \frac{1}{V}(\frac{\partial V}{\partial T})_P$ is very sensitive to anharmonicity [22]. Discrepancies between *ab initio* results using the QHA and experimental data at high temperatures are often attributed to anharmonicity. However, the influence of thermal electronic excitations on this quantity in metallic systems is rarely addressed. To address this influence, we examine this property at 300 K where anharmonicity is expected to be insignificant.

As shown in Figs. 2 and 4, TQHA and EIM approach give quite similar values for entropy, free energy, and pressure for ε-Fe up to ~4000 K. Therefore, we expect them to offer similarly good results for other thermodynamic properties as well. Here, we examine the difference between $\alpha^{\rm EIM}(P, 300\ {\rm K})$, $\alpha^{\rm TIP}(P, 300\ {\rm K})$, and $\alpha^{\rm QHA}(P, 300\ {\rm K})$. Here, $\alpha^{\rm TIP}(P, 300\ {\rm K})$ is computed using T-independent phonons obtained with $T_{\rm el} =$ 300 K, and $\alpha^{\rm QHA}(P, 300\ {\rm K})$ used $T_{\rm el} = 300$ K to compute $F_{\rm st}(V, T)$ also. The last procedure is standard and is inspired by the small $T_{\rm el}$ dependence of the VDoS. Figure 5 shows these quantities and compares them with $\alpha^{\rm exp}(P, 300\ {\rm K})$ [50].

First, at these relatively low temperatures, the $T_{\rm el}$ dependence of the VDoS has little impact on this quantity, with $\alpha^{\rm EIM}$ and $\alpha^{\rm TIP}$ results being quite similar. Second, the $T_{\rm el}$ dependence of $F_{\rm st}(V, T)$, not included in $\alpha^{\rm QHA}$, strongly affects this quantity. Because the calculation of α involves a T derivative, the influence of $T_{\rm el}$ on $F_{\rm st}(V, T)$ and consequently on $P_{\rm st}(V, T)$ or $V(P, T)$ considerably affects $\alpha(P, T)$, even at low temperatures, as previously pointed out [30].

The inset in Fig. 5 compares $\alpha^{\rm EIM}(P, T)$ and $\alpha^{\rm TIP}(P, T)$ with $\alpha^{\rm exp}(P, T)$ at much higher pressures and temperatures. Here, $\alpha^{\rm exp}(P, T)$ was obtained using a semi-empirical EoS for ε-Fe [13], which was computed based on DAC experiments at ambient temperature, Hugoniot data [51], and some *ab initio* modeling [48]. *Ab initio* results by Sha and Cohen [4] are also presented for comparison. First, $\alpha^{\rm EIM}(P, T)$ agrees with $\alpha^{\rm exp}(P, T)$ the best. Second, $\alpha^{\rm EIM}(P, T)$ and $\alpha^{\rm TIP}(P, T)$ increasingly deviate from each other with increasing temperatures, but the deviation decreases with increasing pressure. This indicates that the T dependence of phonon frequencies, whether originating in electronic excitations of phonon-phonon interactions, becomes relevant at these high temperatures. Since the discrepancy between $\alpha^{\rm EIM}(P, T)$ and $\alpha^{\rm exp}(P, T)$ decreases with increasing pressure, anharmonicity should be the source of this discrepancy, as indicated by $P_{\rm vib}$ calculations (Fig. 4). Further improvement in the agreement between these quantities is expected by replacing phonon frequencies with quasiparticle frequencies [21,52], more properly describing the T dependence of the VDoS.

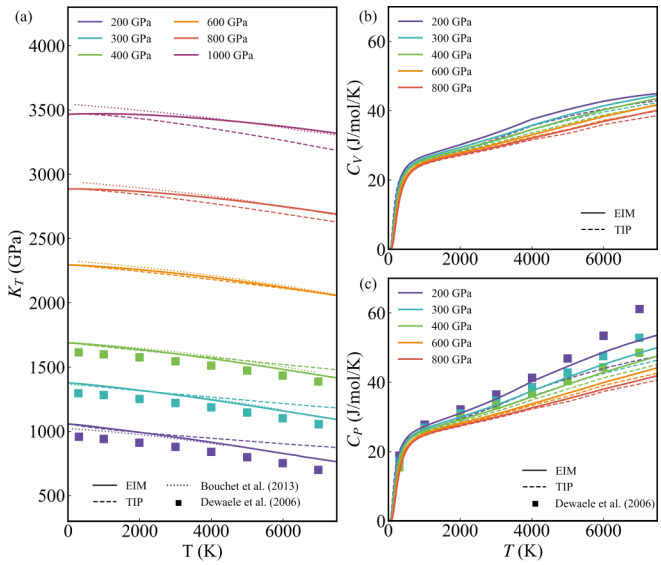

FIG. 6. (a) Isothermal bulk modulus K_T, (b) isochoric specific heat C_V, and (c) isobaric specific heat C_P of ε-Fe. Solid lines are obtained using the entropy integration method (EIM) method; dashed lines are obtained using the temperature-independent phonon (TIP) scheme with phonons calculated with $T_{\rm el} = 300$ K. Dotted lines in (a) are from a previous *ab initio* study [22]. Symbols are results of a thermodynamic analysis [60] based on equations of state (EoS) measured in diamond anvil cell (DAC) experiments [13].

D. Other thermodynamic properties

With previously obtained quantities, we compute the internal energy $E = F + TS$ and other thermodynamic properties such as the isothermal bulk modulus $K_T = -V(\frac{\partial P}{\partial V})_T$ and isochoric and isobaric specific heat, i.e., $C_V = (\frac{\partial E}{\partial T})_V$ and $C_P = C_V + \alpha^2 TVK_T$, as shown in Fig. 6. We compare semi-empirically "modeled" experimental data [13] with results of the EIM and TIP schemes, the latter being common and much more computationally efficient.

As shown in Fig. 6(a), $K_T^{\rm EIM}(P,T)$ results agree well with $K_T^{\rm exp}(P,T)$, as do results from a previous calculation [22]. Differences depend slightly on temperature and pressure. It increases with increasing temperature and decreasing pressure. This behavior is usually the symptom of anharmonicity. Second, the deviation between $K_T^{\rm EIM}(P,T)$ and $K_T^{\rm TIP}(P,T)$ is quite visible >4000 K at all pressures, while the nature of this deviation changes with increasing pressure. This implies the $T_{\rm el}$ dependence of the VDoS is impactful. Third, $K_T^{\rm EIM}(P,T)$ also agrees very well with *ab initio* MD results [22] $K_T^{\rm MD}(P,T)$ that account for anharmonic effects up to 6000 K and 400 GPa. At higher pressures, a noticeable deviation develops between $K_T^{\rm EIM}(P,T)$ and $K_T^{\rm MD}(P,T)$. The origin of this discrepancy is unclear, but it could be technical issues such as the choice of pseudopotentials.

Here, $C_V(P,T)$ and $C_P(P,T)$ shown in Figs. 6(b) and 6(c) indicate very similar trends: $C_{V,P}^{\rm EIM}(P,T)$ agrees better with modeled experimental data [13] than $C_{V,P}^{\rm TIP}(P,T)$. The difference between $C_{V,P}^{\rm EIM}(P,T)$ and $C_{V,P}^{\rm exp}(P,T)$ increases at higher temperatures and decreases at higher pressures. Similarly, the difference between $C_{V,P}^{\rm EIM}(P,T)$ and $C_{V,P}^{\rm TIP}(P,T)$ increases at higher temperatures and decreases at higher pressures. As expected, the T dependence of $C_{V,P}^{\rm EIM}(P,T)$ is nearly linear at high temperatures, but we notice a deviation from linearity ~4000 K at 200 GPa, which decreases at higher pressures. Such a deviation reflects the sampling of the nonparabolic electronic density of states of ε-Fe around the Fermi level at these temperatures.

In summary, >4000 K, we see indications of anharmonic effects on thermodynamic properties at pressures >200 GPa. Here, C_V and C_P suggest anharmonic effects decrease with increasing pressure.

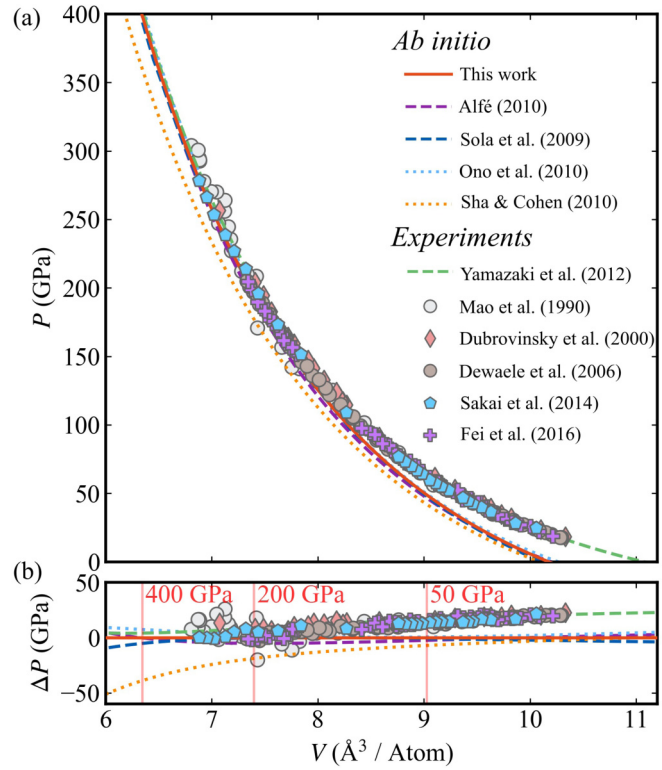

FIG. 7. (a) Comparison between experimental and theoretical equations of state (EoS) of ε-Fe at 300 K. Symbols and dashed green line were obtained in static compression experiments on a diamond anvil cell (DAC): Mao *et al.* [11], Dubrovinsky *et al.* [12], Dewaele *et al.* [13], Sakai *et al.* [54], Fei *et al.* [55], and Yamazaki *et al.* [56]. The latter was reported as parameters of a Birch–Murnaghan third-order (BM3) [61] equation of state (EoS). Theoretical results include *ab initio* PBE-MD results by Alfè [9], quantum Monte Carlo (QMC) by Sola *et al.* [2], static PBE results by Ono *et al.* [53], PBE-LMTO results by Sha and Cohen [4]. Results reported as EoS parameters (BM3 and Vinet *et al.* [62]) are shown as dashed and dotted lines, respectively. (b) Pressure difference vs V, $\Delta P(V)$, with regard to our entropy integration method (EIM) results. Vertical lines at $P = 50$, 200, and 400 GPa indicate volumes used in our EIM calculations.

E. EoS at 300 K

Figure 7 shows the calculated compression curve of ε-Fe compared with other *ab initio* calculations [2,4,9,53] and DAC experimental data [11–13,54–56] at 300 K. Here, $V^{\rm EIM}(P, 300\ {\rm K})$ agrees well with most *ab initio* predictions,

especially at the highest pressures, except with the results of Sha and Cohen [4]. All spin-unpolarized calculations using the PBE-GGA deviate from $V^{\exp}(P, 300\ \mathrm{K})$ curves below ∼100 GPa. Above ∼100 GPa, which is the pressure range of concern here, essentially all *ab initio* predictions show very good agreement with experimental data. There is also some deviation between various $V^{\exp}(P, 300\ \mathrm{K})$ datasets, especially at the highest pressures. Thus, *ab initio* predictions are highly reproducible and reliable at such high pressures and should provide good constraints on the properties of ε-Fe. Combining this conclusion with conclusions from previous sections, it seems that, if T_{el} effects are properly included also in VDoS calculations, the EIM approach can offer reliable properties of ε-Fe without including anharmonic effects up to 360 GPa and ∼4000 K, somewhat shy from inner core temperatures. Reaching inner core temperatures requires inclusion of anharmonic effects as done in other *ab initio* calculations (e.g., Refs. [2,20,22]).

F. Isentropic EoS

The following results are obtained using the EIM scheme. To generate an isentropic EoS, we first compute the adiabatic gradient as follows:

$$\left(\frac{\partial T}{\partial P}\right)_S = \frac{\alpha V T}{C_P}, \tag{5a}$$

where α is the thermal expansion coefficient, and C_P is the isobaric specific heat. The adiabatic temperature profile is then obtained by integrating the adiabatic gradient with appropriate initial conditions:

$$T = T_0 + \int_{P_0}^{P_1} \left(\frac{\partial T}{\partial P}\right)_s dP. \tag{5b}$$

We assume the initial conditions $P_0 = 60$ GPa and $T_0 = 1050$ K to reproduce the experimental ramp compression data on Fe obtained at the NIF [16]. We then compute the volume/density throughout this $T-P$ profile. We use three different valence-core electron interaction potentials: EPAW [32], Jollet-Torrent-Holzwarth (JTH) [33], and Garrity-Bennett-Rabe-Vanderbilt (GBRV) [34], to assess the impact of this approximation at very high pressures, a significant point of concern. The vibrational contribution to the free energy is computed using VDoS calculated using the EPAW method. The impact of pseudopotential changes on F_{vib} is of second order compared with the impact on F_{st} [57].

The possible $T-P$ profiles reported in the NIF experiment and our calculated profiles are shown in the Fig. 8 inset. The predicted isentropes are well within the range of temperatures expected in the NIF experiments. Our predicted isentropic $P-\rho$ EoS using all three potentials also agree reasonably well with the NIF data up to 1000 GPa [Fig. 8(b)].

The JTH potential results agree best with the experimental data, but it does not reproduce the all-electron static EoS. The GBRV and EPAW predictions agree well with each other. EPAW reproduces better the all-electron EoS [32]. This seems to suggest that the unsatisfactory performance of these good EPAW and GBRV potentials is related to the uncertain temperature in the NIF experiments at the highest pressure. The experimental compression curve may not follow precisely

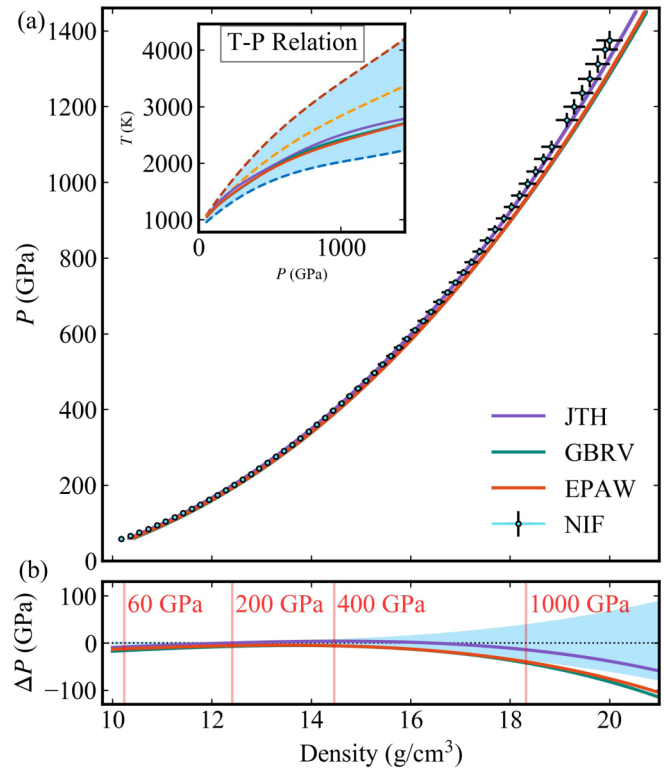

FIG. 8. (a) Isentropic $P-\rho$ equations of state (EoS) of ε-Fe. Small circles with uncertainties are the National Ignition Facility (NIF) data [16]. Solid lines correspond to entropy integration method (EIM) results and different pseudopotentials in the static part of the calculation: evolutionary projector augmented wave (EPAW) potential [32] (red line), Jollet-Torrent-Holzwarth (JTH) potential [33] (purple line), and Garrity-Bennett-Rabe-Vanderbilt (GBRV) ultra-soft potential [34] (green line). The vibrational contribution to the free energy in these calculations was obtained using the EPAW method. Inset: the temperature in the NIF data: red dashed line corresponds to an intermediate strength model for Fe; yellow dashed line is a low-strength model; blue dashed line corresponds to shock compression to 60 GPa before ramp compression to pressures >1 TPa; blue shaded region corresponds to the possible temperature range achieved in the NIF experiment. Red, purple, and green solid lines show adiabatic $T-P$ relations obtained using the EIM method and EPAW, JTH, and GBRV potentials, respectively. (b) Pressure difference with regard to the NIF data (circles with uncertainties), $\Delta P(\rho)$: blue shaded region shows possible uncertainty in the NIF data; red, purple, and green lines correspond to our EIM results using different potentials in the static part of the calculations along their respective adiabats shown in the inset in (a). Red vertical lines show corresponding pressures in the NIF data.

an isentrope, and the temperature achieved in the experiments might be slightly higher than the temperature range represented in the Fig. 8 inset. On the other hand, we have not included anharmonic effects in our calculations, even though the isentropic temperature profile does not seem to reach temperatures at which this issue should be of concern. Nevertheless, anharmonicity should be included for greater accuracy in such calculations and for a more conclusive diagnostic on the origin of the discrepancy between the measured and calculated isentropic $P-\rho$ profile.

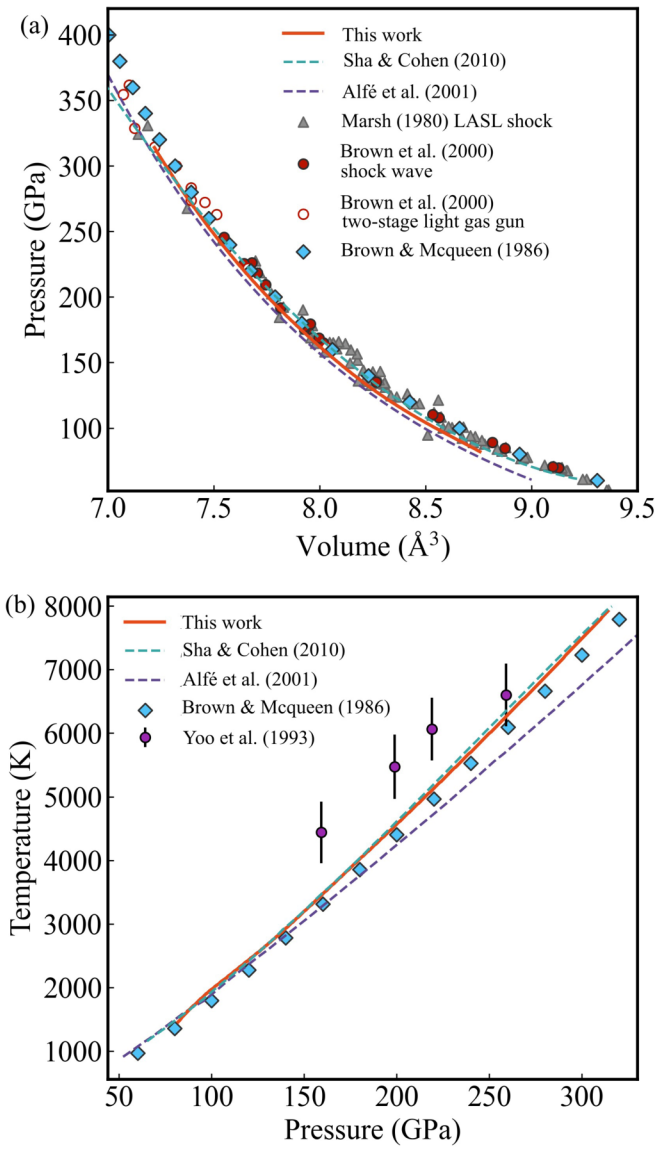

FIG. 9. (a) P vs V and (b) T vs P along the Hugoniot. Solid red lines are entropy integration method (EIM) results using evolutionary projector augmented wave (EPAW) potentials; dashed blue lines are *ab initio* results by Sha and Cohen [4]; dashed purple lines are *ab initio* results by Alfè *et al.* [48]. Symbols correspond to experimental data: gray triangles from Ref. [59], filled red circles and the hollow circles from Ref. [51], filled blue diamonds from Ref. [14], purple circles with error bars from Ref. [15].

G. EoS on the Hugoniot

Shockwave data gives Hugoniot EoS in a wide pressure-temperature range, i.e., at least up to 250 GPa and 5000 K for ε-Fe. Conservation of mass, momentum, and energy in experiments produce the Rankine–Hugoniot formula [1,58]

$$\tfrac{1}{2}P_H(V_0 - V_H) = E_H - E_0, \tag{6}$$

where P is pressure, V is volume, and E is internal energy. The subscript H on V, P, and E stands for Hugoniot. We calculate the $T-P$ path such that the Hugoniot relation in Eq. (6) is observed. Our predicted EIM EoS along the Hugoniot and the associated $T-P$ path are shown in Fig. 9. Our EIM predictions agree well with experiments [14,51,59] and other *ab initio* calculations [4,48] up to ~4000 K and ~200 GPa.

IV. CONCLUSIONS

We have implemented an accurate free energy calculation scheme based on the entropy integration that applies equally to situations where phonon frequencies are T dependent or independent. Several free energy computation schemes have been compared, showing that the EIM is the most accurate, especially when dealing with metallic systems. Using ε-Fe as a test case, we have explored the detailed performance of this method to compute several thermodynamic properties. For metallic systems, the effect of thermal electronic excitations on the vibrational free energy is not significant at up to ~4000 K at ~200 GPa in the present case, which justifies the use of T-independent frequencies in many practical situations. However, accurate predictions of the thermodynamic properties of metals require computations of the Mermin free energy, the static energy component, in a $T_{\rm el}$ continuum. This effect is clearly demonstrated in the calculation of the thermal expansion coefficient of ε-Fe at 300 K. Anharmonic effects do require consideration of T-dependent frequencies (quasiparticle frequencies) to be predictive.

The computed vibrational entropy, vibrational pressure, thermal expansion coefficient, and equation of state are in overall good agreement with measurements at least up to 4000 K at 200 GPa when thermal electronic excitations are properly accounted for. Beyond these conditions, anharmonicity needs to be addressed in these calculations, which can be accomplished by replacing phonon frequencies with T-dependent phonon quasiparticle frequencies [24]. We expect this procedure to be predictive in computing properties of hot iron cores in exoplanets.

ACKNOWLEDGMENTS

This paper was supported in part by the US Department of Energy Award No. DESC0019759 and in part by the National Science Foundation Award No. EAR-1918126 (R.M.W.). This paper used the Extreme Science and Engineering Discovery Environment (XSEDE), USA, which was supported by the National Science Foundation, USA, Grant No. ACI-1548562. Computations were performed on Stampede2, the flagship supercomputer at the Texas Advanced Computing Center (TACC), The University of Texas at Austin, generously funded by the National Science Foundation (NSF) Award No. ACI-1134872.

[1] J. P. Poirier, *Introduction to the Physics of the Earth's Interior*, 2nd edition (Cambridge University Press, Cambridge, 2000).

[2] E. Sola, J. P. Brodholt, and D. Alfè, Equation of state of hexagonal closed packed iron under Earth's core conditions from

quantum Monte Carlo calculations, Phys. Rev. B **79**, 024107 (2009).

[3] L. Stixrude, Structure of Iron to 1 Gbar and 40 000 K, Phys. Rev. Lett. **108**, 055505 (2012).

[4] X. Sha and R. E. Cohen, First-principles thermal equation of state and thermoelasticity of hcp Fe at high pressures, Phys. Rev. B **81**, 094105 (2010).

[5] L. Vocadlo, G. A. de Wijs, G. Kresse, M. Gillan, G. D. Price, L. Vocadlo, and G. A. de Wijs, First principles calculations on crystalline and liquid iron at Earth's core conditions, Faraday Discuss. **106**, 205 (1997).

[6] D. Alfe, M. J. Gillan, L. Vocadlo, J. Brodholt, and G. D. Price, The *ab initio* simulation of the Earth's core, Philos. Trans. A Math. Phys. Eng. Sci. **360**, 1227 (2002).

[7] G. Steinle-Neumann, L. Stixrude, and R. E. Cohen, First-principles elastic constants for the hcp transition metals Fe, Co, and Re at high pressure, Phys. Rev. B **60**, 791 (1999).

[8] L. Vočadlo, J. Brodholt, D. Alfè, M. J. Gillan, and G. D. Price, *Ab initio* free energy calculations on the polymorphs of iron at core conditions, Phys. Earth Planet. Inter. **117**, 123 (2000).

[9] D. Alfè, Iron at Earth's core conditions from first principles calculations, Rev. Mineral. Geochem. **71**, 337 (2010).

[10] A. B. Belonoshko, S. Arapan, and A. Rosengren, An *ab initio* molecular dynamics study of iron phases at high pressure and temperature, J. Phys. Condens. Matter **23**, 485402 (2011).

[11] H. K. Mao, Y. Wu, L. C. Chen, and J. F. Shu, Static compression of iron to 300 GPa and Fe(0.8)Ni(0.2) alloy to 260 GPa—implications for composition of the core, J. Geophys. Res. **95**, 21737 (1990).

[12] L. S. Dubrovinsky, S. K. Saxena, F. Tutti, S. Rekhi, and T. LeBehan, *In Situ* X-Ray Study of Thermal Expansion and Phase Transition of Iron at Multimegabar Pressure, Phys. Rev. Lett. **84**, 1720 (2000).

[13] A. Dewaele, P. Loubeyre, F. Occelli, M. Mezouar, P. I. Dorogokupets, and M. Torrent, Quasihydrostatic Equation of State of Iron above 2 Mbar, Phys. Rev. Lett. **97**, 215504 (2006).

[14] J. M. Brown and G. Mcqueen, Phase transitions, Griineisen parameter, and elasticity, J. Geophys. Res. **91**, 7485 (1986).

[15] C. S. Yoo, N. C. Holmes, M. Ross, D. J. Webb, and C. Pike, Shock Temperatures and Melting of Iron at Earth Core Conditions, Phys. Rev. Lett. **70**, 3931 (1993).

[16] R. F. Smith, D. E. Fratanduono, D. G. Braun, T. S. Duffy, J. K. Wicks, P. M. Celliers, S. J. Ali, A. Fernandez-Pañella, R. G. Kraus, D. C. Swift, G. W. Collins, and J. H. Eggert, Equation of state of iron under core conditions of large rocky exoplanets, Nat. Astron. **2**, 452 (2018).

[17] J. Wang, R. F. Smith, J. H. Eggert, D. G. Braun, T. R. Boehly, J. Reed Patterson, P. M. Celliers, R. Jeanloz, G. W. Collins, and T. S. Duffy, Ramp compression of iron to 273 GPa, J. Appl. Phys. **114**, 023513 (2013).

[18] A. P. van den Berg, D. A. Yuen, K. Umemoto, M. H. G. Jacobs, and R. M. Wentzcovitch, Mass-dependent dynamics of terrestrial exoplanets using *ab initio* mineral properties, Icarus **317**, 412 (2019).

[19] A. B. Belonoshko, J. Fu, T. Bryk, S. I. Simak, and M. Mattesini, Low viscosity of the Earth's inner core, Nat. Commun. **10**, 2483 (2019).

[20] T. Sun, J. P. Brodholt, Y. Li, and L. Vocadlo, Melting properties from *ab initio* free energy calculations: Iron at the Earth's inner-core boundary, Phys. Rev. B **98**, 224301 (2018).

[21] T. Sun, D.-B. Zhang, and R. M. Wentzcovitch, Dynamic stabilization of cubic $CaSiO_3$ perovskite at high temperatures and pressures from *ab initio* molecular dynamics, Phys. Rev. B **89**, 094109 (2014).

[22] J. Bouchet, S. Mazevet, G. Morard, F. Guyot, and R. Musella, *Ab initio* equation of state of iron up to 1500 GPa, Phys. Rev. B **87**, 094102 (2013).

[23] S. deGironcoli, Lattice dynamics of metals from density-functional perturbation theory, Phys. Rev. B **51**, 6773 (1995).

[24] Y. Lu, T. Sun, P. Zhang, P. Zhang, D. Zhang, and R. M. Wentzcovitch, Premelting hcp to bcc Transition in Beryllium, Phys. Rev. Lett. **118**, 145702 (2017).

[25] N. D. Mermin, Thermal properties of the inhomogeneous electron gas, Phys. Rev. **137**, A1441 (1965).

[26] R. M. Wentzcovitch, J. L. Martins, and P. B. Allen, Energy versus free-energy conservation in first-principles molecular dynamics, Phys. Rev. B **45**, 11372 (1992).

[27] T. Sun, K. Umemoto, Z. Wu, J.-C. Zheng, and R. M. Wentzcovitch, Lattice dynamics and thermal equation of state of platinum, Phys. Rev. B **78**, 024304 (2008).

[28] G. Grimvall, *Thermophysical Properties of Materials* (Elsevier, Amsterdam, North Holland, 1999).

[29] D. C. Wallace, *Thermodynamics of Crystals* (Dover, Mineola, 1972).

[30] P. B. Allen, Theory of thermal expansion: Quasi-harmonic approximation and corrections from quasi-particle renormalization, Mod. Phys. Lett. B **34**, 2050025 (2020).

[31] P. Giannozzi *et al.*, QUANTUM ESPRESSO: A modular and open-source software project for quantum simulations of materials, J. Phys. Condens. Matter **21**, 395502 (2009).

[32] K. Sarkar, M. Topsakal, N. A. W. Holzwarth, and R. M. Wentzcovitch, Evolutionary optimization of PAW data-sets for accurate high pressure simulations, J. Comput. Phys. **347**, 39 (2017).

[33] F. Jollet, M. Torrent, and N. Holzwarth, Generation of projector augmented-wave atomic data: A 71 element validated table in the XML format, Comput. Phys. Commun. **185**, 1246 (2014).

[34] K. F. Garrity, J. W. Bennett, K. M. Rabe, and D. Vanderbilt, Pseudopotentials for high-throughput DFT calculations, Comput. Mater. Sci. **81**, 446 (2014).

[35] J. P. Perdew, K. Burke, and M. Ernzerhof, Generalized Gradient Approximation Made Simple, Phys. Rev. Lett. **77**, 3865 (1996).

[36] H. J. Monkhorst and J. D. Pack, Special points for Brillouin-zone integrations, Phys. Rev. B **13**, 5188 (1976).

[37] R. M. Wentzcovitch, Invariant molecular-dynamics approach to structural phase transitions, Phys. Rev. B **44**, 2358 (1991).

[38] R. M. Wentzcovitch, J. L. Martins, and G. D. Price, *Ab Initio* Molecular Dynamics with Variable Cell Shape: Application to $MgSi0_3$, Phys. Rev. Lett. **70**, 3947 (1993).

[39] S. Baroni, S. de Gironcoli, A. Dal Corso, and P. Giannozzi, Phonons and related crystal properties from density-functional perturbation theory, Rev. Mod. Phys. **73**, 515 (2001).

[40] T. Qin, Q. Zhang, R. M. Wentzcovitch, and K. Umemoto, qha: A Python package for quasiharmonic free energy calculation for multi-configuration systems, Comput. Phys. Commun. **237**, 199 (2019).

[41] R. Lubbers, H. F. Grunsteudel, A. I. Chumakov, and G. Wortmann, Density of phonon states in iron at high pressure, Science **287**, 1250 (2000).

[42] H. K. Mao, J. Xu, V. V. Struzhkin, J. Shu, R. J. Hemley, W. Sturhahn, M. Y. Hu, E. E. Alp, L. Vocadlo, D. Alfe, G. D. Price, M. J. Gillan, M. Schwoerer-Bohning, D. Hausermann, P. Eng, G. Shen, H. Giefers, R. Lubbers, and G. Wortmann, Phonon density of states of iron up to 153 Gigapascals, Science **292**, 914 (2001).

[43] G. Shen, W. Sturhahn, E. E. Alph, J. Zhao, T. S. Toellnner, V. B. Prakapenka, Y. Meng, and H. R. Mao, Phonon density of states in iron at high pressures and high temperatures, Phys. Chem. Miner. **31**, 353 (2004).

[44] J.-F. Lin, W. Sturhahn, J. Zhao, G. Shen, H. Mao, and R. J. Hemley, Sound velocities of hot dense iron: Birch's law revisited, Science **308**, 1892 (2005).

[45] C. A. Murphy, J. M. Jackson, and W. Sturhahn, Experimental constraints on the thermodynamics and sound velocities of hcp-Fe to core pressures: Thermoelasticity of hcp-Fe to 171 GPa, J. Geophys. Res. Solid Earth **118**, 1999 (2013).

[46] T. B. Massalski and D. E. Laughlin, The surprising role of magnetism on the phase stability of Fe (ferro), Calphad **33**, 3 (2009).

[47] C. A. Murphy, J. M. Jackson, W. Sturhahn, and B. Chen, Melting and thermal pressure of hcp-Fe from the phonon density of states, Phys. Earth Planet. Inter. **188**, 114 (2011).

[48] D. Alfè, G. D. Price, and M. J. Gillan, Thermodynamics of hexagonal-close-packed iron under Earth's core conditions, Phys. Rev. B **64**, 045123 (2001).

[49] P. I. Dorogokupets and A. R. Oganov, Equations of state of Al, Au, Cu, Pt, Ta, and W and revised ruby pressure scale, Dokl. Earth Sci. **410**, 1091 (2006).

[50] O. L. Anderson, L. Dubrovinsky, S. K. Saxena, and T. LeBihan, Experimental vibrational Grüneisen ratio values for ϵ-iron up to 330 Gpa at 300 K, Geophys. Res. Lett. **28**, 399 (2001).

[51] J. M. Brown, J. N. Fritz, and R. S. Hixson, Hugoniot data for iron, J. Appl. Phys. **88**, 5496 (2000).

[52] Z. Zhang, D.-B. Zhang, T. Sun, and R. M. Wentzcovitch, phq: a Fortran code to compute phonon quasiparticle properties and dispersions, Comput. Phys. Commun. **243**, 110 (2019).

[53] S. Ono, T. Kikegawa, N. Hirao, and K. Mibe, High-pressure magnetic transition in hcp-Fe, Am. Mineral. **95**, 880 (2010).

[54] T. Sakai, S. Takahashi, N. Nishitani, I. Mashino, E. Ohtani, and N. Hirao, Equation of state of pure iron and $Fe_{0.9}Ni_{0.1}$ alloy up to 3 Mbar, Phys. Earth Planet. Inter. **228**, 114 (2014).

[55] Y. Fei, C. Murphy, Y. Shibazaki, A. Shahar, and H. Huang, Thermal equation of state of hcp-iron: Constraint on the density deficit of Earth's solid inner core, Geophys. Res. Lett. **43**, 6837 (2016).

[56] D. Yamazaki, E. Ito, T. Yoshino, A. Yoneda, X. Guo, B. Zhang, W. Sun, A. Shimojuku, N. Tsujino, T. Kunimoto, Y. Higo, and K. I. Funakoshi, P-V-T equation of state for ϵ-iron up to 80 GPa and 1900 K using the Kawai-type high pressure apparatus equipped with sintered diamond anvils, Geophys. Res. Lett. **39**, 20 (2012).

[57] R. M. Wentzcovitch, Y. G. G. Yu, and Z. Q. Wu, in *Theoretical and Computational Methods in Mineral Physics: Geophysical Applications*, edited by R. Wentzcovitch and L. Stixrude (Mineralogical Soc Amer & Geochemical Soc, Chantilly, 2010), p. 59.

[58] O. L. Anderson, *Equations of State of Solids for Geophysics and Ceramic Science* (Oxford University Press, Oxford, 1995).

[59] S. P. Marsh, *LASL Shock Hugoniot Data* (University of California Press, Berkeley, 1980).

[60] A. B. Belonoshko, P. I. Dorogokupets, B. Johansson, S. K. Saxena, and L. Koci, *Ab initio* equation of state for the body-centered-cubic phase of iron at high pressure and temperature, Phys. Rev. B **78**, 104107 (2008).

[61] F. Birch, Finite elastic strain of cubic crystals, Phys. Rev. **71**, 809 (1947).

[62] P. Vinet, J. Ferrante, J. H. Rose, and J. R. Smith, Compressibility of solids, J. Geophys. Res. **92**, 9319 (1987).